Materials Today Energy 7 (2018) 199–207

Contents lists available at ScienceDirect

Materials Today Energy

journal homepage: www.journals.elsevier.com/materials-today-energy/

Exciton and lattice dynamics in low-temperature processable $CsPbBr_3$ thin-films

Christoph Wolf [a], Tae-Woo Lee [b, *]

[a] Department of Materials Science and Engineering, Pohang University of Science and Technology (POSTECH), Pohang, Gyungbuk 37673, Republic of Korea
[b] Department of Materials Science and Engineering, Research Institute of Advanced Materials, Seoul National University, 1 Gwanak-ro, Gwanak-gu, Seoul 08826, Republic of Korea

ARTICLE INFO

Article history:
Received 21 June 2017
Received in revised form
14 August 2017
Accepted 10 September 2017
Available online 8 October 2017

Keywords:
Electron–phonon coupling
Lead-halide perovskite
Exciton binding energy
Temperature-dependent spectroscopy

ABSTRACT

Lead-halide based perovskite semiconductors have recently attracted significant attention owing to their rapidly increasing efficiency in solar cells and light-emitting devices. Organic–inorganic lead halide perovskites have gained popularity due to their low-temperature solution processability, low electronic defect density and low structural and thermal disorder. Nonetheless, their single crystals suffer from lower carrier mobility (~10–100 $cm^2 V^{-1} s^{-1}$) than those in inorganic semiconductors and slow radiative recombination rates, with average lifetimes exceeding one μs. Recently, $CsPbBr_3$, an all-inorganic lead-bromide perovskite also attracted great attention due to its high thermal stability and fast radiative recombination. Therefore, it is required to explore the exciton and lattice dynamics of solution processed $CsPbBr_3$ thin films. Here, we show that $CsPbBr_3$ exhibits an electron–phonon coupling strength (~70 meV) comparable with its organic–inorganic hybrid perovskite counterpart $CH_3NH_3PbBr_3$ (~60 meV). The main source of electron–phonon coupling was identified to be the longitudinal-optical phonon mode of the Pb–Br lattice vibration at ~20 meV. Carrier recombination studies by temperature-dependent steady-state and time-resolved photoluminescence revealed that recombination occurred from lattice-bound carriers at room-temperature and in inert atmosphere. Carrier lifetimes are short and show a distinct temperature-dependence. All findings are supported by first-principles calculations in the framework of density-functional theory.

1. Introduction

Lead-halide ($PbBr_2$, $PbCl_2$, PbI_2)-based perovskite structures with the generic formula $APbX_3$ (A = organic or inorganic cation, X = halide) have attracted a great attention due to rapid increase of electro-optical performance especially in solar cells and LEDs [1,2]. Early studies already indicated that the PbX_6 octahedra dominates the optical properties with the band extrema being hybridized states of lead and halide orbitals [3].

An intriguing property is the low-temperature, solution processability of all commonly used $APbX_3$ perovskites which allows processing at temperatures generally considered compatible with flexible substrates and printing processes, thought to overcome limitations of generally expensive high-temperature, high vacuum processing currently employed in the semiconductor industry. The so far most studied variant of $APbX_3$ contain an organic methylammonium (MA, CH_3NH_3) or formamidimium (FA, $HC(NH_2)$) cation on the A-site and the halide is either iodine for solar cell applications [2,4] or chlorine and bromine for light-emitting diodes [5,6] owing to the strong band-gap dependence of the compound which gradually decreases along the halide group Cl > Br > I (3 eV > 2.3 eV > 1.6 eV) [7], almost irrespective of the A-cation. Combinations of the halide are known to span the whole visible spectrum, which has been explored for light-emitting applications as well [8]. Binding energy of the electron–hole pair or exciton is reported in the range of 2–60 meV and a decrease of the binding energy with temperature has been reported by some groups [9,10].

Currently two stringent limitations of organic–inorganic hybrid materials have emerged: The first is the limited carrier mobility in both, highly crystalline and polycrystalline samples [11]. The discrepancy between long carrier lifetimes and low carrier mobilities can be rationalized by strong coupling of the charge carriers to the lattice [12–14]. The second is the long carrier lifetime, driving high efficiency solar-cells but drastically limit efficient radiative

* Corresponding author.
E-mail addresses: twlees@snu.ac.kr, taewlees@gmail.com (T.-W. Lee).

http://dx.doi.org/10.1016/j.mtener.2017.09.010
2468-6069/

recombination in light-emitting diodes (LED). A recent report has linked these long lifetimes to the motion of anisotropic MA and FA cations, but the effect is absent in isotropic cesium (Cs)-based perovskites [15]. Calculation has revealed that in $CsPbI_3$ slow hole cooling due to coupling to the Pb–I vibrations is the origin of slow recombination dynamics and should thereby be practically independent of the A-site cation [16]. It has, however, recently been reported that the polar structure of these A-site occupants might play a role in the formation of excitons and subsequent dissociation into charge carriers [17].

These findings motivate to replace the polar, anisotropic, organic A-site cation with the non-polar isotropic Cs. The resulting $CsPbBr_3$ does not significantly differ from the organic–inorganic hybrid perovskites (MA or $FAPbBr_3$) in terms of band-gap [18], but the distinctively different screening behavior of the excited carriers [15], strongly favors fast radiative recombination in $CsPbBr_3$. The material is further known to be processable at low-temperatures around 300 K [19,20]. In addition, the completely inorganic compound has a higher temperature stability compared to the organic–inorganic hybrids and high-purity single crystals can be grown by conventional methods at high temperatures (700 °C) [21]. LED device fabrication is at an early stage but simple one-layer devices incorporating $CsPbBr_3$ as emitter material already rival previously reported devices based on $MAPbBr_3$ with record luminescence values of 176,000 cd m^{-2} and peak external quantum efficiencies of ~6% [6,22,23].

Here, we aim to detail the physics underlying photon absorption and emission and the interaction of carrier and lattice in solution processed $CsPbBr_3$ by temperature-dependent UV/VIS absorption and photoluminescence (PL) spectroscopy and density-functional (DFT) calculation. Temperature-dependent PL data allowed the identification of two PL quenching channels, one being assigned to the facile thermal ionization of excitons due to their small exciton binding energy (40 meV) in good agreement with DFT calculation and literature and the other suspected to be a halide vacancy defect state. We analyzed the electron–phonon coupling from temperature dependent PL broadening, which stems from a longitudinal-optical (LO) phonon mode of 20 meV, found in the Raman spectrum and by density functional perturbation calculation. From absorption data we are able to determine the band-gap shift, which is shown to follow a blue-shift with increasing temperature. The Urbach disorder energy extracted from the exponential onset of absorption reveals low structural disorder and dominantly thermal disorder which, again, can be attributed to the same LO phonon mode. The total disorder at room-temperature is less than 40 meV. The Fröhlich coupling constant for an LO-coupled polaron is $\alpha \sim 1.1$, comparable to many polar inorganic semiconductors. The electron–phonon coupling constant obtained from PL broadening of $CsPbBr_3$ is ~70 meV, comparable to that of their organic–inorganic hybrid counterpart $CH_3NH_3PbBr_3$ (60 meV). Analysis of the photoluminescence lifetime using stretched exponentials revealed short lifetimes and a high order parameter $\beta \approx 0.7$ at low temperatures, indicative of efficient, excitonic recombination. The order parameter shows a distinct temperature dependence which can be linked to the influence of thermal disorder on the recombination of carriers. Overall $CsPbBr_3$ shows comparable electron–phonon coupling, and more efficient carrier-recombination than $MAPbBr_3$ whilst maintaining solution-processability with low electronic disorder.

2. Results and discussion

This section is organized as follows: Section 2.1 through 2.3 will present experimental findings of temperature dependent PL and absorption spectroscopy and their analysis. Section 2.4 will show ab-initio calculations on $CsPbBr_3$ and discuss the agreement between experiment and calculation. In Section 2.5 we analyzed $CsPbBr_3$ in the frame-work of the Froehlich polaron model.

2.1. Photoluminescence spectroscopy

The choice of fabrication condition for low-temperature, solution processed samples is especially crucial in the field of hybrid perovskites. Dimethyl sulfoxide (DMSO) is an excellent solvent for the precursor materials but its interaction with the perovskite materials are not entirely clear [24]. The high boiling point of DMSO (lit. 189 °C) makes it hard to remove by conventional techniques without damaging the sample. We fabricated perovskite samples from single-source precursors and applied a wide range of annealing temperatures between 90 °C and 210 °C. The temperature dependent steady state PL data is shown in Fig. 1.

The PL data at the lowest annealing temperature (90 °C) clearly showed thermally stimulated PL in an intermediate temperature range which can be attributed to a trapping–detrapping mechanism [25]. For $T_A > 130$ °C that behavior gradually vanished and the PL decay behavior stabilized. X-ray diffraction patterns collected for all annealing temperatures (Fig. S1 in the supporting information) indicate that thermal annealing is not necessary to fully react $CsBr + PbBr_2 \rightarrow CsPbBr_3$ in stoichiometric precursors and we attribute the change in PL emission to the removal of residual solvents and possibly recrystallization. We chose 170 °C annealing temperature which results in stable emission behavior It is remarkable that this low processing temperature lead to PL properties that are comparable to high-temperature, vacuum processed

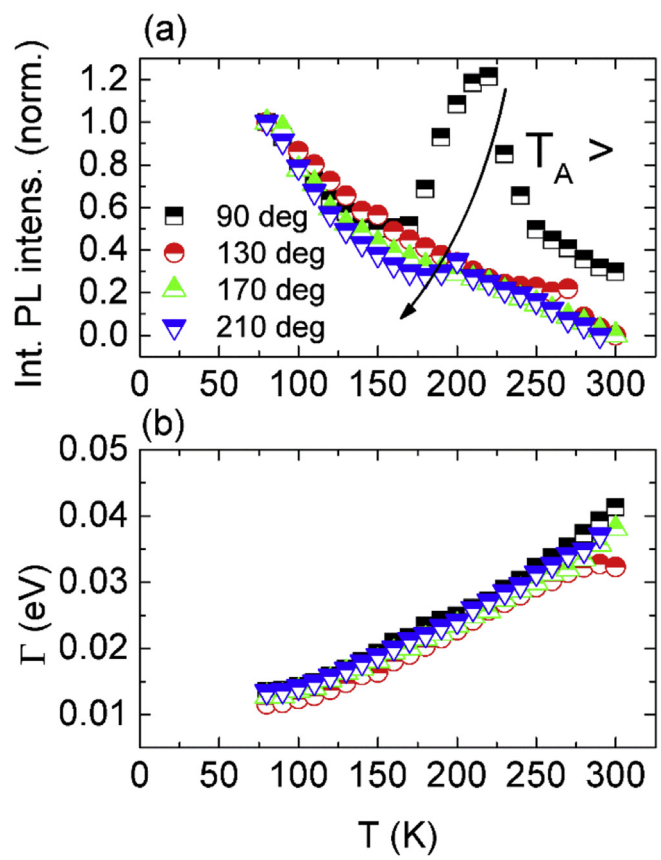

Fig. 1. (a) Integrated PL intensity as a function of temperature for samples annealed at the indicated temperature. (b) Gaussian width of the PL emission as function of temperature. The width is clearly less sensitive to annealing temperature than the amplitude indicating that emission stems from the same recombination mechanism.

$CsPbBr_3$ [21]. Features known to stem from amorphous $CsPbBr_3$ were absent in our samples [19], and the film showed good and homogeneous coverage and PL emission (Fig. S2).

Using 170 °C annealed samples, we perform temperature-dependent time-integrated PL spectroscopy in the range between 77 K and 300 K. Fig. 2 shows the resulting temperature-dependent PL data. The spectra are well fitted by a single Gaussian ($R^2 > 0.99$) and free of side-peaks. The integrated PL intensity closely follows a two-term Arrhenius equation (Equation (1)).

$$I(\mathrm{T}) = \frac{I_0}{A_1 \exp\left(\frac{-E_1}{k_B T}\right) + A_2 \exp\left(\frac{-E_2}{k_B T}\right) + 1}, \tag{1}$$

where the temperature dependence of the integrated peak intensity, $I(T)$ is expressed as a fitting constant I_0, and two exponential terms where the pre-factor A_i can be interpreted as the density of a PL quenching mechanism with associated activation energy E_i. The fitting results are $A_1 = 25\pm5$, $E_1 = 40\pm5$ meV, $A_2 \approx 10^{10}$, $E_2 = 500\pm250$ meV. We note that A_2, E_2 cannot be precisely determined in the available temperature range. The phenomenological nature of the Arrhenius fitting function does not allow to identify the underlying cause of each quenching channel directly [26]. We assign the first decay energy to thermal dissociation of excitons with literature values of the exciton binding energy in the range of $E_b \approx 40 - 60$ meV [27], which we confirm by first principles calculation (see Section 2.4).

The second deactivation channel is most likely an ionized defect, owing to the relatively high activation energy and considering that halide ions are known to be very mobile in these perovskite materials [28–31]. At low temperatures, PL quenching is accurately described by exciton dissociation, and close to room temperature, recombination from free carriers becomes gradually more susceptible to defects. This is further evidenced by the strong influence of reactive oxygen atmosphere at room temperature, dramatically boosting the PL yield (details in supporting note S1) [32].

The blue-shift of the emission peak with temperature is commonly observed in $APbX_3$ perovskites and supported by first-principles calculations and experiments [3,33,34]. We can confirm the blue-shift of band-gap by DFT calculation (Fig. S4). The resulting band-widening with increased lattice parameter agrees with our data qualitatively at temperatures below 200 K. The S-shape of the PL peak shift (Fig. 2c) indicates thermal expansion dominating at low temperature is followed by pinning of the emission energy center. In accordance with previous literature results for $MAPbBr_3$ and $CsPbBr_3$ [35,36], this effect can be attributed to renormalization of the band-gap due to interaction of carriers with the lattice (electron–phonon coupling). Considering thermal expansion and electron–phonon coupling, the temperature dependence of the band-gap can be described by (Equation (2)) [23,37].

$$E_c(T) = E_0 + AT - a\left(1 + \frac{2}{\exp\left(\frac{\Theta}{T}\right) - 1}\right), \tag{2}$$

where $E_c(T)$ is the temperature dependent PL peak center with a constant energy E_0, the thermal expansion term AT and a Bose–Einstein factor describing the lattice-coupling of magnitude a and temperature Θ, related to the average phonon energy $E_{Ph} = k_B\Theta$. The fit results in $E_0 = 2.45\pm0.1$ eV, $A = (2.6\pm0.2)\times 10^{-4}$ eVK^{-1}, $a = 0.14\pm0.03$ and the Einstein-temperature of $\Theta \approx 740$ K. The corresponding energy ($k_B\Theta \approx 60$ meV) is higher than the highest phonon mode in $CsPbBr_3$, which leads us to believe the pinning effect should be attributed to the ionization of defects, which would adapt a similar functional form and cannot be discerned from this experiment alone. The zero-temperature peak position is given by $E_0 - a = 2.45 - 0.14 = 2.30$ eV. Our results are in excellent agreement with measurements performed on the

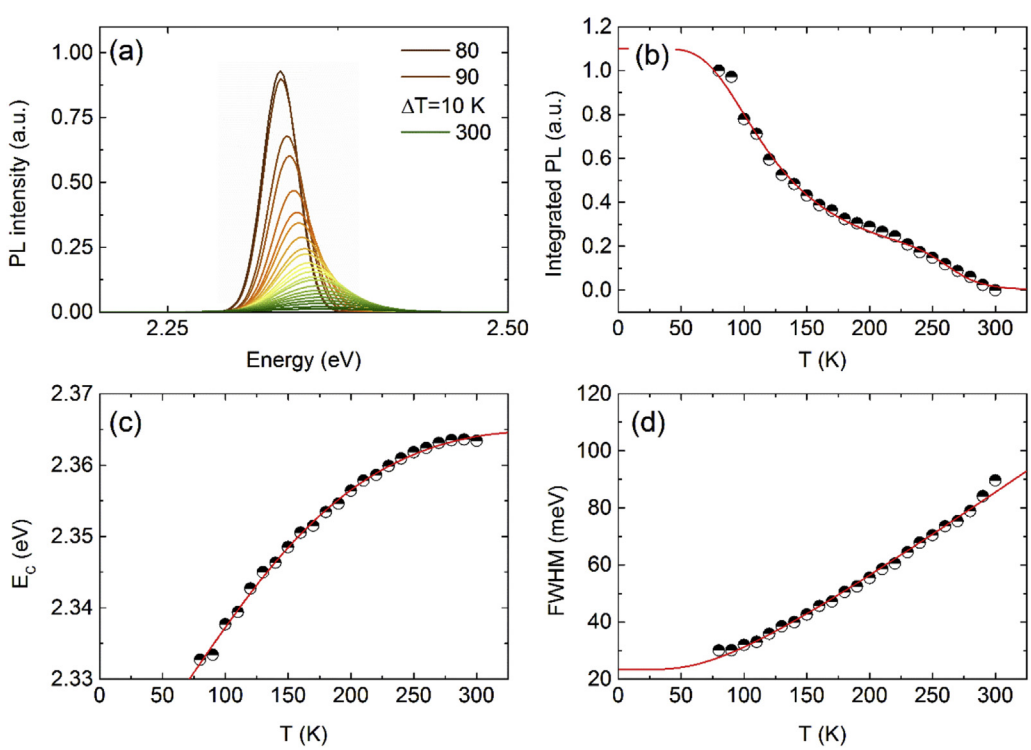

Fig. 2. (a) Temperature dependent PL spectra. (b) Integrated PL intensity as a function of temperature. The solid line is a fit of a two-term Arrhenius equation (Equation (1)). (c) Blue-shift of the emission center with Equation (2) as fitting function. (d) The broadening of PL in terms of Gaussian width (Equation (3)).

temperature dependent PL of quantum dots of the same material [35].

To reveal the dominant interaction between lattice and carrier we analyze the thermal PL line-width (full width at half maximum, FWHM) broadening. The temperature-dependence of the PL is generally described by (Equation (3)) [38].

$$\Gamma(\mathrm{T}) = \Gamma_0 + \gamma_{ph}T + \frac{\Gamma_{LO}}{\left(\exp\left(\frac{E_{LO}}{k_BT}\right) - 1\right)} + \Gamma_{imp}\exp\left(\frac{-E_D}{k_BT}\right), \quad (3)$$

where $\Gamma(\mathrm{T})$, Γ_0, $\Gamma_{LO}, \Gamma_{imp}$ are the temperature-dependent PL FWHM, the intrinsic line-width at absolute temperature 0 K, the coupling strength (the average energy times number of phonons) of the LO phonon, and the broadening arising from impurities with ionization energy E_D, respectively. The acoustic phonon coupling is neglected here ($\gamma_{ph} \approx 0$) but has been reported for the related $FAPbBr_3$ to lead to broadening <18 meV at room temperature [12]. In our experimentally temperature range limited to temperatures below 300 K scattering from ionized impurities does not seem to contribute to the broadening and we set $\Gamma_{imp} = 0$.

The average energy $E_{LO} = \hbar\omega$ attributed to broadening is $E_{LO} = 20\pm5$ meV, $\Gamma_o = 23\pm1$ meV, $\Gamma_{LO} = 73\pm2$ meV. The phonon energy is in agreement with literature data for $CsPbBr_3$ grown by Bridgman method [39], (165 cm^{-1}, $PbBr_6$ vibration) we find indeed a mode close to 20 meV (161 cm^{-1}) by Raman spectroscopy (Fig. S5) of our solution processed samples which we can attribute to the LO phonon mode by calculation of the vibrational spectrum.

2.2. Temperature-dependent, time-resolved PL spectroscopy

Performing temperature-dependent PL lifetime spectroscopy by time-correlated single photon counting (TCSPC) reveals relatively short PL lifetimes and a monotonous temperature dependence below 220 K. A wide variety of fitting functions have been employed in literature to extract PL lifetimes but with increasing complexity, multi-exponential decay components are hard to analyze with respect to the underlying physics. Considering the disordered nature of our polycrystalline films a discrete distribution of carrier lifetimes as dictated by a multi-exponential fit seems unlike and we use a stretched exponential (Kohlrausch function) to describe our TCSPC data instead [40,41]. The reliability function of the stretched exponential $I(\mathrm{t}) = \exp\left(-\left(\frac{t}{t_1}\right)^{\beta}\right)$ is used to fit the TCSPC data. The underlying assumption is that the carrier lifetime has a continuous distribution with characteristic time t_1 and width, which is described by the stretching parameter $0 \le \beta \le 1$, where 1 is a perfectly ordered single decay channel (corresponding to single-exponential, perfectly excitonic decay) and the lifetime distribution gets broader as β decreases. The average lifetime is then $\tau = \frac{t_1}{\beta}\overline{\Gamma}(1/\beta)$, where $\overline{\Gamma}$ is the gamma function. We find two separate regimes for the lifetime data separated by 220 K. Below 220 K $t_1 = 0.446$ ns and β continuously decreases with temperature which shows a temperature-dependent behavior $\beta(\mathrm{T}) \approx 0.73/(1 + 6 \times \exp(-58\ meV/T))$. Above 220 K $t_1 = 0.19$ ns and β further decreases to about 0.47 at RT. Temperature-dependent TCSPC data and the temperature dependence of β is shown in Fig. 3. At low temperature (80 K) the short average lifetime and high β value indicate efficient radiative recombination with excitonic character. The continuous decrease of β with increasing temperature leads to the emergence of slow recombination rates (see Figs. S6 and S7) and correspondingly longer average lifetimes. We note that the whilst the monotonous increase of average lifetime below and above 220 K can be explained by the increase of thermal disorder of the system

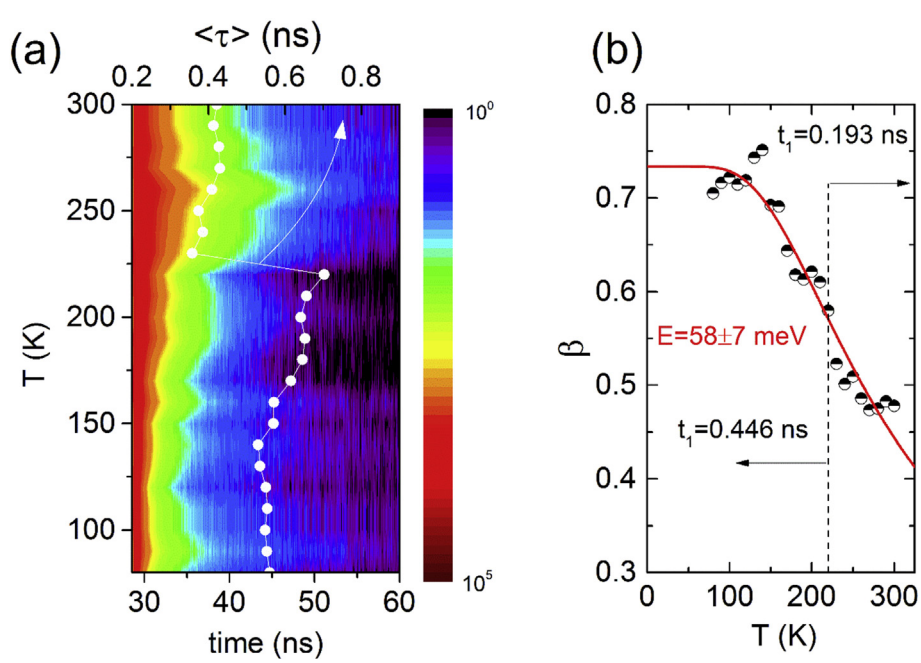

Fig. 3. Results of the PL lifetime measurements. (a) PL intensity as function of time and temperature with an overlay of average PL lifetime (bullets correspond to upper x-axis with values of $\tau = \frac{t_1}{\beta}\overline{\Gamma}\left(\frac{1}{\beta}\right)$); with increasing temperature the average lifetime continuously increases up to 220 K where a sudden change in PL decay behavior occurs. The data between 80 K and 220 K are fitted with a fixed lifetime component of $t_1 = 0.446$ ns, above 220 K the data required a change of lifetime component to $t_1 = 0.193$ ns. The fit quality for 300 K data is poor ($X^2 \sim 2.2$) and is only shown for the sake of completeness. (b) The corresponding values of the stretching parameter β following an Arrhenius behavior indicated by the solid line with a characteristic energy of ~58 meV.

[42,43], the abrupt change of the radiative lifetime t_1 at 220 K remains elusive at this stage and calls for further investigation in future works.

2.3. Temperature-dependent absorption spectroscopy

The results of temperature-dependent absorption data are shown in Fig. 4. Absorption data is frequently analyzed in the framework of Elliott's theory of absorption which allows to separate the excitonic and band-to-band continuum contribution to the absorption spectrum [44,45]. We extract band-gap shift E_g, exciton binding energy E_B (shown in Fig. S7) and the width of the exciton absorption line Γ. Further, the onset of absorption data carries information about the disorder, commonly called Urbach-Energy (E_U) [46]. To extract the disorder energy the onset of the absorption data on a logarithmic scale is fitted linearly and the inverse of the slope is the Urbach (disorder) energy. The Urbach energy is related to the steepness parameter $\sigma(T) = k_B T/E_U$ that is linked to the phonon energy $\hbar\omega$ by the Dow–Redfield model (Equation (4)) [47].

$$\sigma(T) = \sigma_0 \frac{2k_B T}{\hbar\omega} \tanh\left(\frac{\hbar\omega}{2k_B T}\right). \tag{4}$$

A least-squares fit of Equation (4) to the data reveals an average phonon energy $\hbar\omega = 25\pm8$ meV. $\sigma_0 = 0.77\pm0.01$ is a temperature independent constant (usually of order unity) and $k_B T$ the thermal energy at temperature T. We explicitly note that all absorption data on the logarithmic scale intersect in a common point (the Urbach focus) of 2.28 eV (Fig. S8), which is a prerequisite for the applicability of this model [48]. The Urbach energy can be partitioned into a temperature independent, structural disorder and a thermal contribution. A wide variety of models exist with a large degree of freedom [49], but we opt for a simple model introduced by Cody (Equation (5)) [50].

$$E_U(T) = \frac{k_B T}{\sigma_0}\left[\frac{1+P}{2} + \frac{N}{\exp\left(\frac{\Theta}{T}\right) - 1}\right], \tag{5}$$

where P, N denote the structural disorder and thermally excited disorder contribution, respectively. The temperature Θ is theoretically proportional to the Debye temperature, but agreement is known to be sometimes poor due to the underlying assumption of this model making Θ temperature independent [51]. In our data fitting results in $P \approx 0$ and $N \approx 1$, which indicates low structural and dominant thermal disorder. The characteristic temperature is $\Theta = 300\pm80$ K. This results in an absolute value of disorder energy at room temperature of $E_U \approx 36$ meV, comparable to previous results in related hybrid-perovskites [52,53]. The temperature-trend of the band-gap is in good agreement with thermal expansion of the lattice up to 200 K but shows renormalization most likely due to strong electron–phonon coupling. The results of fitting Equation (2) to the absorption data is shown in Table 1. The broadening of the absorption peak basically follows the same mechanism as for PL and yields similar numbers when treated with Equation (3) as shown in Table 1. The exciton binding energy is in the expected range for bromide-based perovskites and lies around 60 meV over the whole temperature range (see supporting Fig. S7). We have previously shown the variation of binding energy extraction from deconvolution and spread of values in literature [53].

A single energy of $E_{LO} = 20\pm5$ meV can be used to fit broadening in PL and absorption data (see Table 1) leading us to believe the Pb–Br LO phonon mode is dominating the charge–lattice interaction in this material.

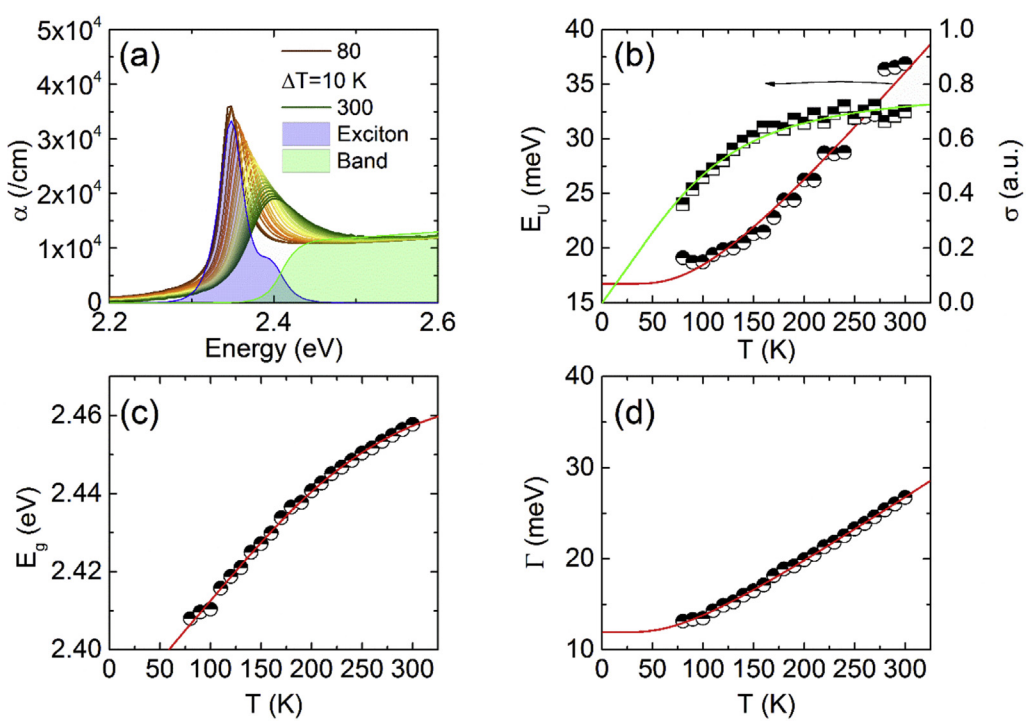

Fig. 4. (a) Temperature dependent absorption data and schematic deconvolution in exciton and band-contribution. (b) The Urbach disorder energy from the onset of absorption (left axis) and steepness parameter (right axis). The solid fits are Equations (4) and (5). (c) The temperature-dependence of the band-gap as extracted from deconvolution. It displays evidence of thermal lattice expansion and electron–phonon renormalization of the gap at elevated temperature (Equation (2)). (d) Broadening of the exciton peak and a broadening function as described by Equation (3).

2.4. Ab-initio calculations on $CsPbBr_3$

2.4.1. Effective carrier masses

We calculated the band-structure of the orthorhombic unit cell (details on the computational methods are given in the methods section). The resulting band-structure plot along high-symmetry lines are shown in Fig. 5. The effective masses close to the Γ-point are $m_h^* = [-0.0861, -0.112, -0.112]$ (in units of the electron rest-mass) for holes and $m_e^* = [0.089, 0.085, 0.75]$ for electrons in principal directions $[k_x, k_y, k_z]$. The low carrier mass anisotropy is reflected in the similar dispersion along $\Gamma - X$, $\Gamma - Y$ and $\Gamma - Z$ in the band-structure plot. Taking the harmonic mean results in effective masses of $m_h^* = 0.105$ and $m_e^* = 0.083$. This results in an reduced mass of $\mu = \frac{m_h^* m_e^*}{m_h^* + m_e^*} \approx 0.05$. Neglecting many-body interactions and thermal effects in effective mass theory allows to estimate the binding energy of the exciton as $E_b = 13.6\mu\varepsilon^{-2}$, where ε is the (effective) dielectric constant [54]. Since the dielectric function varies significantly with frequency it is common to use a value somewhere between the static and high-frequency limit, so that $\varepsilon_\infty \le \varepsilon \le \varepsilon_0$. Our calculations in the framework of density functional perturbation theory (DFPT, details in the methods section) give a high-frequency limit (ion clamped) dielectric constant of ε_∞ =4.7. Using Cochran's law the static dielectric constant is $\varepsilon_0 = 15.1$ when considering the two highest energy LO/TO modes (see Fig. S9 for details) [55]. Measurements for the related $CsPbCl_3$ perovskite resulted in $\varepsilon \approx 3$, [56] and the static dielectric constant trend in $CsPbX_3$ has previously been studied and follows a gradual increase 4.07 < 4.96 < 6.32 for X = Cl, Br and I, respectively [27]. This allows to estimate the limit of exciton binding energy in $CsPbBr_3$ to be ≈30 meV using a dielectric constant of 4.7. This energy agrees with the energy assigned to PL decay channel $E_1 = 40$ meV. The resulting exciton radius is $r_B = 0.53\varepsilon_r\mu^{-1} \approx 5$ nm, in good agreement with experimental observations where strong confinement is observed in quantum-dots with diameters less than 7–10 nm [27].

2.4.2. Phonons and electron–phonon coupling

Strong electron–LO–phonon coupling has previously been experimentally and computationally demonstrated for hybrid lead-halide perovskites [12,17]. In $CsPbBr_3$ the band-extrema are hybridized Pb(s,p) and Br (s,p) states (see Figs. 5 and 6 (a)). We calculated the phonon-dispersion using DFPT (Fig. 6 (c)). This confirms the presence of an LO phonon mode at 22 meV (176 cm^{-1}) shown in Fig. 6 (c), in excellent agreement with the fitting results of an LO coupling model of $\hbar\omega_{LO} = 20\pm5$ meV (Table 1) and Raman data (Fig. S5). That phonons contribute significantly (up to 60 meV at 300 K) to the self-energy of the charges near the valence band maximum is evident from Fig. 6 (e). Overall the estimation of broadening from the self-energy Σ of conduction and valence band (CB, VB) as FWHM$\approx Z \times 2(\Sigma_{CB} + \Sigma_{VB})$, with Z~0.5 at 0 K for the related material $MAPbBr_3$ [12]. The quasiparticle renormalization factor shows acceptable agreement between calculation and measurement at 300 K.

2.5. Fröhlich coupling constant of $CsPbBr_3$

Motivated by the strong electron phonon interaction evident from experiment and ab-initio calculation we calculate the electron–phonon coupling constant α by applying the mesoscopic Fröhlich polaron model to $CsPbBr_3$ [17,57]. In brief, for a large polaron interacting with LO-phonons the coupling constant α is given by (Equation (7)) [58].

$$\alpha = \frac{e^2}{\hbar c}\sqrt{\frac{m_b c^2}{2\hbar\omega_{LO}}}\left(\frac{1}{\varepsilon_\infty} - \frac{1}{\varepsilon_0}\right), \tag{7}$$

where $e, c, \hbar$ denote electron charge, speed of light and Planck constant, respectively. m_b is the effective carrier mass deduced from the band-structure calculation (Section 2.3), ω_{LO} the angular frequency of the LO phonon mode (20 meV) and ε_∞ (4.7) and ε_0 (15) are the electronic and static relative dielectric constants obtained from DFPT. This results in $\alpha_e = 1.22$, $\alpha_h = 1.05$, with e, h indicating hole and electron, respectively. The corresponding polaron masses are given by $m_{e,h}^\star \approx 1 + \alpha_{e,h}/6 + 0.0236\alpha_{e,h}^2 = 1.2$, 1.2 (in units of the respective effective mass, e.g. the polaron gains 20% mass) [59]. These values are identical to values reported for the related material $CH_3NH_3PbI_3$ (~20% mass enhancement) [60]. The size of these polarons can be estimated as $R_p \approx \frac{3}{2}\left(\frac{3}{2\alpha}\frac{\hbar}{m\omega_{LO}}\right)^{1/2}$, i.e. strongly increasing as $\alpha \to 0$ [61]. We note that our coupling constants are at the limit of the large-polaron regime (generally denoted as $\alpha < 2$). The resulting polaron radius using an LO energy of 20 meV and $\alpha =$ 1.1 is $R_p \approx 3.5$ nm, which corresponds to several $PbBr_6$ units,

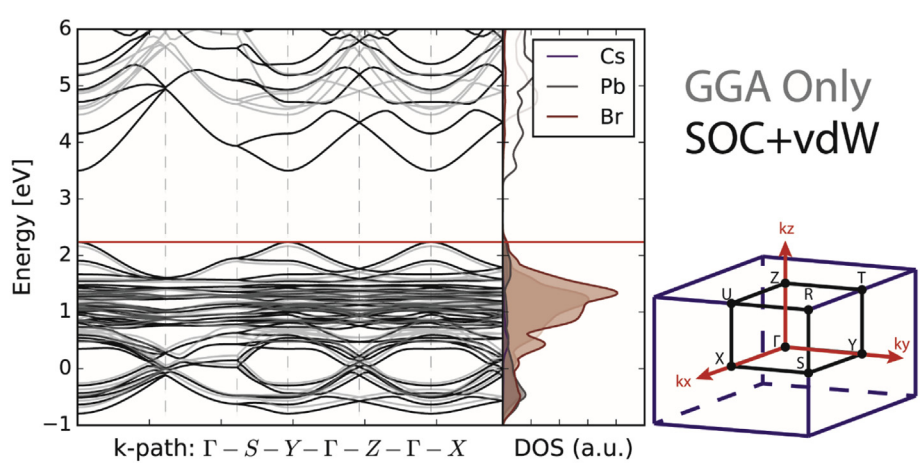

Fig. 5. Band-structure plot of the Kohn-Sham energies along the high-symmetry line of the orthorhombic unit cell (depicted) and the projection of wave-functions (projected density of states, PDOS). The effect of spin–orbit coupling (SOC) and van der Waals (vdW) interaction on the narrowing of the direct gap is evident and leads to a roughly 40% decrease of the bare generalized-gradient approximation (GGA) band-gap of 2.3 eV.

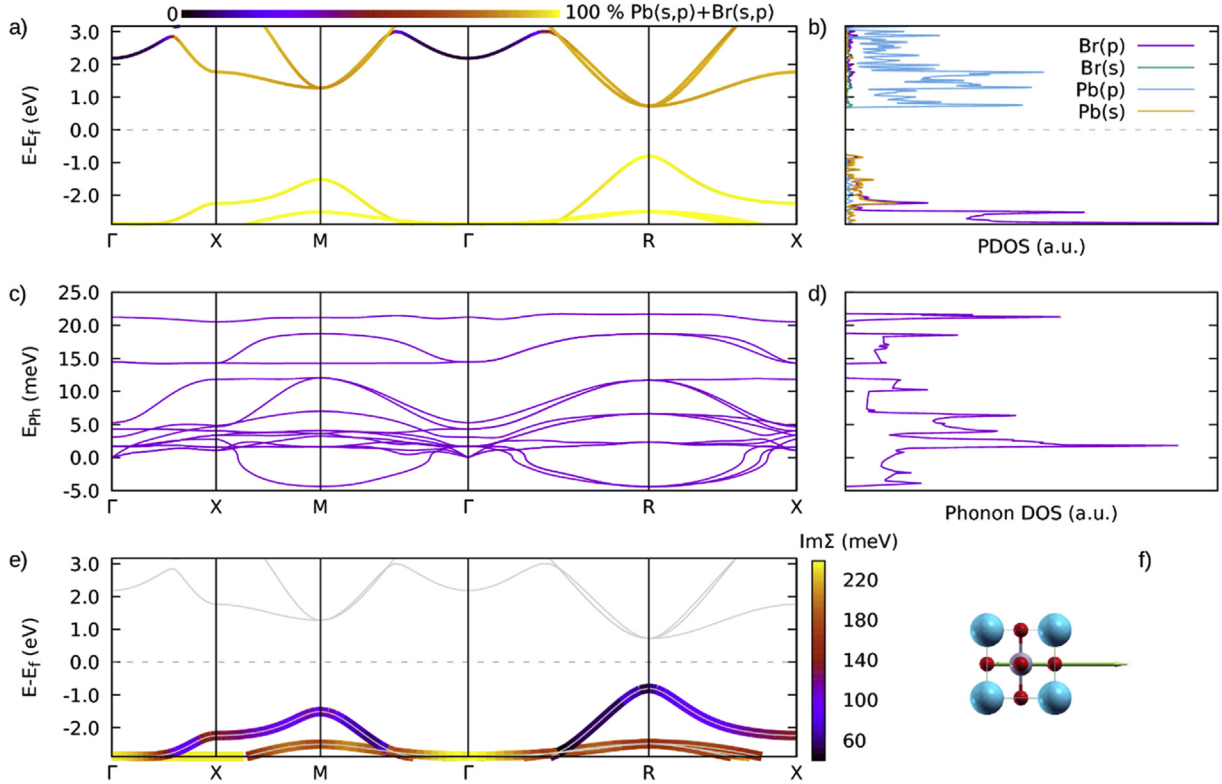

Fig. 6. Results of the calculation of electronic and phonon structure of the cubic $CsPbBr_3$ unit cell. (a) Fat-band representation of the electronic band-structure close to the gap indicating the contribution to the band extrema stemming mainly from an hybridization of Pb(s,p) and Br(p) with negligible contribution of Cs. (b) projected density of states (PDOS) of the electronic band-structure. (c) Phonon-dispersion along the high-symmetry lines. The LO–TO splitting at G between 15 meV and 22 meV is evident. Negative energies correspond to soft-modes [71,72]. (d) Phonon DOS showing a high DOS of the 20 meV mode. (e) Electron self-energy due to interaction with phonons IM(S) in meV superimposed over the electronic band-structure. Close to the transition point the magnitude of self-energy is around 40–60 meV. (f) The LO mode indicated by force-arrows showing the Pb–Br vibration.

Table 1
Summary of the results of the fit of broadening function (Equation (3)) and temperature-dependent shift (Equation (2)) to PL and absorption (abs) data. The uncertainties noted are standard-errors from the fit procedure alone and do not include systematic errors from the experiment.

	Broadening $\Gamma(T) = \Gamma_0 + \gamma_{ph}T + \frac{\Gamma_{LO}}{\left(\exp\left(\frac{E_{LO}}{k_B T}\right)-1\right)}$			Gap-Shift $E_c(T) = E_0 + AT - a\left(1 + \frac{2}{\exp\left(\frac{\Theta}{T}\right)-1}\right)$			
	Γ_0 (meV)	Γ_{LO} (meV)	E_{LO} (meV)	E_0 (eV)	A (10^{-4} eVK^{-1})	a (eV)	Θ (K)
PL	23±1	73±2	20±5	2.45±0.1	2.5±0.2	0.14±0.03	740±80
abs	11±0.4	16±2	18±2	2.64±0.2	3.1±0.2	0.26±0.1	1030±170

justifying the description large polaron. The polaron size is similar to the exciton radius (Section 2.4.1) indicating that the excited state is an exciton-polaron [62].

3. Conclusion

In this work, we have revealed that low-temperature solution processed $CsPbBr_3$ has optical properties that can rival the same material processed in high vacuum and at much higher temperature. The temperature-dependence of photoluminescence is well described by two quenching channels, one ascribed to the thermal dissociation of excitons with a characteristic energy of 40 meV, the second having a much higher energy (>250 meV) and is expected to be related to a halide vacancy defect (V_{Br}). The dominating broadening mechanism in solution-processed $CsPbBr_3$ is through LO phonon coupling. The magnitude of electron–phonon coupling deduced from PL is ~70 meV, comparable to the organic–inorganic hybrid $MAPbBr_3$ (60 meV) [12]. The LO-phonon mode has an energy of ~20 meV which is the Pb–Br vibration mode, present in the Raman spectrum and confirmed by DFPT phonon calculation. Temperature dependence of the band-gap estimated from PL emission peak position and de-convoluted absorption spectra clearly shows initially linear blue-shift, in good agreement with thermal expansion of the lattice below 220 K and a more complex behavior above 200 K. The Urbach disorder energy of the low-temperature processed film is low and amounts to less than 40 meV at RT. Low structural Urbach energy is apparently an intrinsic property of $APbX_3$ perovskites, in good agreement with literature [52,63]. The dominant lattice vibration of the disorder as indicated by the Dow–Redfield model again is ~20 meV leading to the conclusion that all disorder phenomena presented are of the same microscopic origin. The data points to the conclusion that excited carrier exist in the form of Fröhlich polarons with similar effective polaron masses for electrons and holes: $m^{\star}_{h,e} = 1.2$. Our findings, supported by ab-initio calculations, indicate that electron–phonon coupling is an important factor in this material and a exciton-polaron picture of the carriers is justified.

4. Experimental section

4.1. Experimental procedures

Temperature dependent PL and absorption measurements were performed on films spin-coated from single-source precursors in a one-step fabrication process.

Equimolar portions of CsBr (Sigma Aldrich, 99.999%) and $PbBr_2$ (Sigma Aldrich, >98%) were dissolved in DMSO (99.9%, anhydrous Sigma Aldrich) to give a 10 wt.% solution (~0.25 M). Spin coating on cleaned (sonication in acetone, 2-butanol and subsequent boiling in 2-butanol) glass substrates results in 65 nm thick, flat films. Thermal annealing for 10 min at indicated temperature was performed. We explicitly note that the high boiling-point of DMSO seems to demand annealing temperatures that exceed 130 °C in order to exhibit the reported results. All fabrication steps in a dry glovebox (H_2O < 4 ppm).

An Oxford DN2 cryostat (sample in exchange gas) was used to perform all temperature dependent measurements using a custom-made Matlab control program on the Oxford instruments Mercury ITC. After setting a target temperature the control program stabilizes the temperature and equilibrates over 3 min before taking the measurement.

A SCINCO S-3100 multichannel spectrophotometer recorded the absorption spectra which were de-convoluted into the 1S exciton level and the continuous band contribution by Elliott's theory, as recently reported [45]. The procedure is automated using Matlab's optimization routine "fmincon" (constrained optimization). In general, the optimization can be performed unconstrained as it shows excellence convergence within only a few steps.

For steady-state PL experiments a pulsed laser diode (LDH 405 nm controlled with a PDL 800-D, both PicoQuant GmbH, average power <1.6 mW at 40 MHz, spot diameter on sample less than 1 mm) was used for excitation and the PL spectra were collected using a fiber-coupled StellarNet blue wave spectrometer. Using lower excitation density is prohibited by the sensitivity of the detector. For power-dependent PL spectroscopy the continuous-wave (CW) mode of the same laser-diode is used. The laser-power is then varied between 0.4 mW and 54 mW (determined using a laser power-meter, Thorlabs S302C with a nominal power range of 10^{-4} to 2 W). The collected spectra were analyzed using Matlab by fitting a single Gaussian to each spectrum. The reported values for σ correspond to the Gaussian width and are related to the FWHM by FWHM ≈ 2.355 × σ. Constrained fits using Matlab's fmincon routine were used and show excellent convergence with R^2 exceeding 0.99 over the whole temperature range indicating the general Gaussian emission shape.

Time-resolved PL was measured using time-correlated single photon counting with the same laser as above using a pulse peak-to-peak time of 400 ns. Detection of the emitted photon is facilitated by a MCP-PMT (Hamamatsu R3809U-50) after selection of the peak wavelength using a monochromator (Acton SP2150). A PicoHarp 300 (PicoQuant GmbH) is used for photon counting. The instrument response function (IRF) of our setup was measured to be less than 0.6 ns. FluoFit (PicoQuant GmbH) was used for analysis of the decay histograms.

4.2. Ab-initio calculations

We performed first-principles calculations in the framework of density functional theory (DFT) as implemented in Quantum-Espresso (QE 6.0) [64]. For band-structure calculations the orthorhombic unit cell containing 20 atoms [39] was sampled with a 4 × 3 × 4 Γ-centered Monkhorst–Pack (MP) [65] grid using an energy-cutoff of 60 Rydberg and optimized norm-conserving [66] pseudopotentials including spin–orbit-interaction (SOC) where indicated. For Pb the d-orbitals were treated as valence. As mentioned in previous reports SOC and dispersive Grimme van-der Waals (vdW) correction leads to a relative narrowing of the gap with respect to the bare generalized-gradient approximation (GGA) gap, however is necessary to properly describe the band dispersion [33]. For the calculation of the effective mass-tensor we use the stencil-grid method and the effective-mass calculator [67].

Phonon calculations were performed within density functional perturbation theory (DFPT) as implemented in QE 6.0 using the cubic unit cell (high-temperature phase above 130 °C [39]; 5 atoms) for computational efficiency. The relaxed lattice constant is 5.87 Å (literature: 5.874 Å [68], see also Table S2 for a comparison of cubic and orthorhombic phase). SOC was not included in these calculations. The ground-state charge-density was converged with a 6 × 6 × 6 unshifted MP grid and phonon dispersions were calculated on the same grid and then interpolated along high-symmetry lines. LO–TO splitting was included.

For the electron–phonon coupling calculation we closely followed a procedure previously published [12]. In brief, the band-structure is interpolated by Wannier functions and the electron-self energy is then calculated using the EPW package [69,70].

Acknowledgements

The author is indebted to Mr. Minseok Yoo for collecting the Raman spectra of $CsPbBr_3$.

This work was supported by the National Research Foundation of Korea (NRF) grant funded by the Korea government (Ministry of Science,ICT and Future Planning) (NRF-2016R1A3B1908431).

Appendix A. Supplementary data

Supplementary data related to this article can be found at http://dx.doi.org/10.1016/j.mtener.2017.09.010.

References

[1] A. Poglitsch, D. Weber, J. Chem. Phys. 87 (1987) 6373.
[2] A. Kojima, K. Teshima, Y. Shirai, T. Miyasaka, J. Am. Chem. Soc. 131 (2009) 6050–6051.
[3] Y.H. Chang, C.H. Park, K. Matsuishi, J. Korean Phys. Soc. 44 (2004) 889–893.
[4] G.E. Eperon, V.M. Burlakov, P. Docampo, A. Goriely, H.J. Snaith, Adv. Funct. Mater. 24 (2014) 151–157.
[5] Z. Tan, R.S. Moghaddam, M.L. Lai, P. Docampo, R. Higler, F. Deschler, M. Price, A. Sadhanala, L.M. Pazos, D. Credgington, F. Hanusch, T. Bein, H.J. Snaith, R.H. Friend, Nat. Nanotechnol. 9 (2014) 1–6.
[6] H. Cho, S.-H. Jeong, M.-H. Park, Y.-H. Kim, C. Wolf, C.-L. Lee, J.H. Heo, A. Sadhanala, N. Myoung, S. Yoo, S.H. Im, R.H. Friend, T.-W. Lee, Science (80-.) 350 (2015) 1222–1225.
[7] I.E. Castelli, J.M. García-Lastra, K.S. Thygesen, K.W. Jacobsen, APL Mater. 2 (2014) 0–7.
[8] Y.-H. Kim, H. Cho, J.H. Heo, T.S. Kim, N. Myoung, C.L. Lee, S.H. Im, T.-W. Lee, Adv. Mater. 27 (2015) 1248–1254.
[9] Y. Yamada, T. Nakamura, M. Endo, A. Wakamiya, Y. Kanemitsu, IEEE J. Photovoltaics 5 (2015) 401–405.
[10] A. Miyata, A. Mitioglu, P. Plochocka, O. Portugall, J.T.-W. Wang, S.D. Stranks, H.J. Snaith, R.J. Nicholas, Nat. Phys. 11 (2015) 582–587.
[11] T.M. Brenner, D.A. Egger, A.M. Rappe, L. Kronik, G. Hodes, D. Cahen, J. Phys. Chem. Lett. 6 (2015) 4754–4757.
[12] A.D. Wright, C. Verdi, R.L. Milot, G.E. Eperon, M.A. Pérez-Osorio, H.J. Snaith, F. Giustino, M.B. Johnston, L.M. Herz, Nat. Commun. 7 (2016) 11755.
[13] A. Filippetti, A. Mattoni, C. Caddeo, M.I. Saba, P. Delugas, Phys. Chem. Chem. Phys. 18 (2016) 15352–15362.
[14] X.-Y. Zhu, V. Podzorov, J. Phys. Chem. Lett. 6 (2015) 4758–4761.
[15] H. Zhu, K. Miyata, Y. Fu, J. Wang, P.P. Joshi, D. Niesner, K.W. Williams, S. Jin, X.-Y. Zhu, Science (80-.) 353 (2016) 1409–1413.
[16] H. Kawai, G. Giorgi, A. Marini, K. Yamashita, Nano Lett. 15 (2015) 3103–3108.
[17] M. Bokdam, T. Sander, A. Stroppa, S. Picozzi, D.D. Sarma, C. Franchini, G. Kresse, Sci. Rep. 6 (2015) 28618.
[18] C.K. Møller, Nature 182 (1958), 1436–1436.
[19] S. Kondo, T. Sakai, H. Tanaka, T. Saito, Phys. Rev. B 58 (1998) 11401–11407.

[20] Y. Rakita, N. Kedem, S. Gupta, A. Sadhanala, V. Kalchenko, M.L. Böhm, M. Kulbak, R.H. Friend, D. Cahen, G. Hodes, Cryst. Growth Des. 16 (2016) 5717–5725.
[21] M. Sebastian, J.A. Peters, C.C. Stoumpos, J. Im, S.S. Kostina, Z. Liu, M.G. Kanatzidis, A.J. Freeman, B.W. Wessels, Phys. Rev. B Condens. Matter Mater. Phys. 92 (2015) 235210.
[22] J. Li, S.G.R. Bade, X. Shan, Z. Yu, Adv. Mater. 27 (2015) 5196–5202.
[23] H. Cho, C. Wolf, H.-J. Yun, J.-S. Bae, H. Kim, J.-M. Heo, S. Ahn, T.-W. Lee, Adv. Mater. (2017) (accepted).
[24] I. Wharf, T. Gramstad, R. Makhija, M. Onyszchuk, Can. J. Chem. 54 (1976) 3430–3438.
[25] J.K. Srivastava, S. Supe, J. Phys. D Appl. (1989) 1537–1543.
[26] J. Krustok, H. Collan, K. Hjelt, J. Appl. Phys. 81 (1997) 1442–1445.
[27] L. Protesescu, S. Yakunin, M.I. Bodnarchuk, F. Krieg, R. Caputo, C.H. Hendon, R.X. Yang, A. Walsh, M.V. Kovalenko, Nano Lett. 15 (2015) 3692–3696.
[28] J. Schoonman, J. Solid State Chem. 4 (1972) 466–474.
[29] I. Yokota, S. Miyatani, Solid State Ionics 3–4 (1981) 17–21.
[30] J. Mizusaki, K. Arai, K. Fueki, Solid State Ionics 11 (1983) 203–211.
[31] K. Wakamura, Y. Noda, J. Phys. Chem. Solids 62 (2001) 2027–2034.
[32] Y. Tian, M. Peter, E. Unger, M. Abdellah, K. Zheng, T. Pullerits, A. Yartsev, V. Sundström, I.G. Scheblykin, Phys. Chem. Chem. Phys. 17 (2015) 24978–24987.
[33] G.R. Yettapu, D. Talukdar, S. Sarkar, A. Swarnkar, A. Nag, P. Ghosh, P. Mandal, Nano Lett. 16 (2016) 4838–4848.
[34] K. Heidrich, H. Künzel, J. Treusch, Solid State Commun. 25 (1978) 887–889.
[35] K. Wei, Z. Xu, R. Chen, X. Zheng, X. Cheng, T. Jiang, Opt. Lett. 41 (2016) 3821.
[36] D. Niesner, O. Schuster, M. Wilhelm, I. Levchuk, A. Osvet, S. Shrestha, M. Batentschuk, C. Brabec, T. Fauster, Phys. Rev. B 95 (2017) 1–9.
[37] F. Giustino, S.G. Louie, M.L. Cohen, Phys. Rev. Lett. 105 (2010) 1–4.
[38] S. Rudin, T.L. Reinecke, Phys. Rev. B 41 (1990) 3017–3027.
[39] C.C. Stoumpos, C.D. Malliakas, J.A. Peters, Z. Liu, M. Sebastian, J. Im, T.C. Chasapis, A.C. Wibowo, D.Y. Chung, A.J. Freeman, B.W. Wessels, M.G. Kanatzidis, Cryst. Growth Des. 13 (2013) 2722–2727.
[40] A.F. Van Driel, I.S. Nikolaev, P. Vergeer, P. Lodahl, D. Vanmaekelbergh, W.L. Vos, Phys. Rev. B Condens. Matter Mater. Phys. 75 (2007) 35329.
[41] R. Kohlrausch, Ann. Phys. 167 (1854) 179–214.
[42] G. Zatryb, A. Podhorodecki, J. Misiewicz, J. Cardin, F. Gourbilleau, Nanoscale Res. Lett. 6 (2011) 106.
[43] S.M. Wasim, G. Marin, C. Rincon, P. Bocaranda, G.S. Perez, J. Phys. Chem. Solids 61 (2000) 669–673.
[44] Michael Bass, Handbook of Optics, in: third ed.Optical Properties of Materials, Nonlinear Optics, Quantum Optics, vol. IV, McGraw-Hill Professional, New York, Chicago, San Francisco, Lisbon, London, Madrid, Mexico City, Milan, New Delhi, San Juan, Seoul, Singapore, Sydney, Toronto, 2010, ISBN 9780071498920.
[45] N. Sestu, M. Cadelano, V. Sarritzu, F. Chen, D. Marongiu, R. Piras, M. Mainas, F. Quochi, M. Saba, A. Mura, G. Bongiovanni, J. Phys. Chem. Lett. 6 (2015) 4566–4572.
[46] F. Urbach, Phys. Rev. 92 (1953) 1324.
[47] J.D. Dow, D. Redfield, Phys. Rev. B 5 (1972) 594–610.
[48] I. Studenyak, M. Kranj, M. Kurik, Int. J. Opt. Appl. 4 (2014) 76–83.
[49] R. Pässler, Phys. Status Solidi 200 (1997) 155–172.
[50] G.D. Cody, T. Tiedje, B. Abeles, B. Brooks, Y. Goldstein, Phys. Rev. Lett. 47 (1981) 1480–1483.
[51] R.C. Rai, J. Appl. Phys. 113 (2013) 153508.
[52] S. De Wolf, J. Holovsky, S.J. Moon, P. Löper, B. Niesen, M. Ledinsky, F.J. Haug, J.H. Yum, C. Ballif, J. Phys. Chem. Lett. 5 (2014) 1035–1039.
[53] C. Wolf, J.S. Kim, T.-W.W. Lee, ACS Appl. Mater. Interfaces 9 (2017) 10344–10348.
[54] R.J. Elliott, Phys. Rev. 108 (1957) 1384–1389.
[55] W. Cochran, R.A. Cowley, J. Phys. Chem. Solids 23 (1962) 447–450.
[56] O.N. Yunakova, V.K. Miloslavsky, E.N. Kovalenko, V.V. Kovalenko, Funct. Mater. 22 (2015) 175–180.
[57] H. Fröhlich, Adv. Phys. 3 (1954) 325–361.
[58] J.T. Devreese, A.S. Alexandrov, Rep. Prog. Phys. 72 (2009) 66501.
[59] J.T. Devreese, A.S. Alexandrov, 66501 (2009) 1–131.
[60] Z.-G. Yu, J. Phys. Chem. Lett. 7 (2016) 3078–3083.
[61] F.M. Peeters, J.T. Devreese, Phys. Rev. B 31 (1985) 4890–4899.
[62] G. Iadonisi, F. Bassani, Nuovo Cim. D 2 (1983) 1541–1560.
[63] A. Sadhanala, F. Deschler, T.H. Thomas, S.E. Dutton, K.C. Goedel, F.C. Hanusch, M.L. Lai, U. Steiner, T. Bein, P. Docampo, D. Cahen, R.H. Friend, J. Phys. Chem. Lett. 5 (2014) 2501–2505.
[64] P. Giannozzi, S. Baroni, N. Bonini, M. Calandra, R. Car, C. Cavazzoni, D. Ceresoli, G.L. Chiarotti, M. Cococcioni, I. Dabo, A.D. Corso, S. de Gironcoli, S. Fabris, G. Fratesi, R. Gebauer, U. Gerstmann, C. Gougoussis, A. Kokalj, M. Lazzeri, L. Martin-Samos, N. Marzari, F. Mauri, R. Mazzarello, S. Paolini, A. Pasquarello, L. Paulatto, C. Sbraccia, S. Scandolo, G. Sclauzero, A.P. Seitsonen, A. Smogunov, P. Umari, R.M. Wentzcovitch, J. Phys. Condens. Matter 21 (2009) 395502.
[65] J.D. Pack, H.J. Monkhorst, Phys. Rev. B 16 (1977) 1748–1749.
[66] D.R. Hamann, Phys. Rev. B Condens. Matter Mater. Phys. 88 (2013) 1–10.
[67] A. Fonari, C. Sutton, Effective Mass Calculator, 2012. https://github.com/afonari/emc.
[68] R.L. Moreira, A. Dias, J. Phys. Chem. Solids 68 (2007) 1617–1622.
[69] S. Poncé, E.R. Margine, C. Verdi, F. Giustino, arXiv 209 (2016) 116–133.
[70] F. Giustino, M.L. Cohen, S.G. Louie, Phys. Rev. B 76 (2007) 1–19.
[71] F. Brivio, J.M. Frost, J.M. Skelton, A.J. Jackson, O.J. Weber, M.T. Weller, A.R. Goni, A.M.A. Leguy, P.R.F. Barnes, A. Walsh, Phys. Rev. B Condens. Matter Mater. Phys. 92 (2015) 1–8.
[72] Y. Fujii, S. Hoshino, Y. Yamada, G. Shirane, Phys. Rev. B 9 (1974) 4549–4559.